Supplementary Information

Interphase–Microstructure Synergy in Al Foil Anodes Enabled by Ball-Milled Al–CNT Composites

Hee-Tae Jeong, Jun Young Kim and Woo Jin Kim*

Department of Materials Science and Engineering, Hongik University, 94 Wausan-ro, Mapo-gu, Seoul 04066, Republic of Korea.

* Correspondence: kimwj@wow.hongik.ac.kr

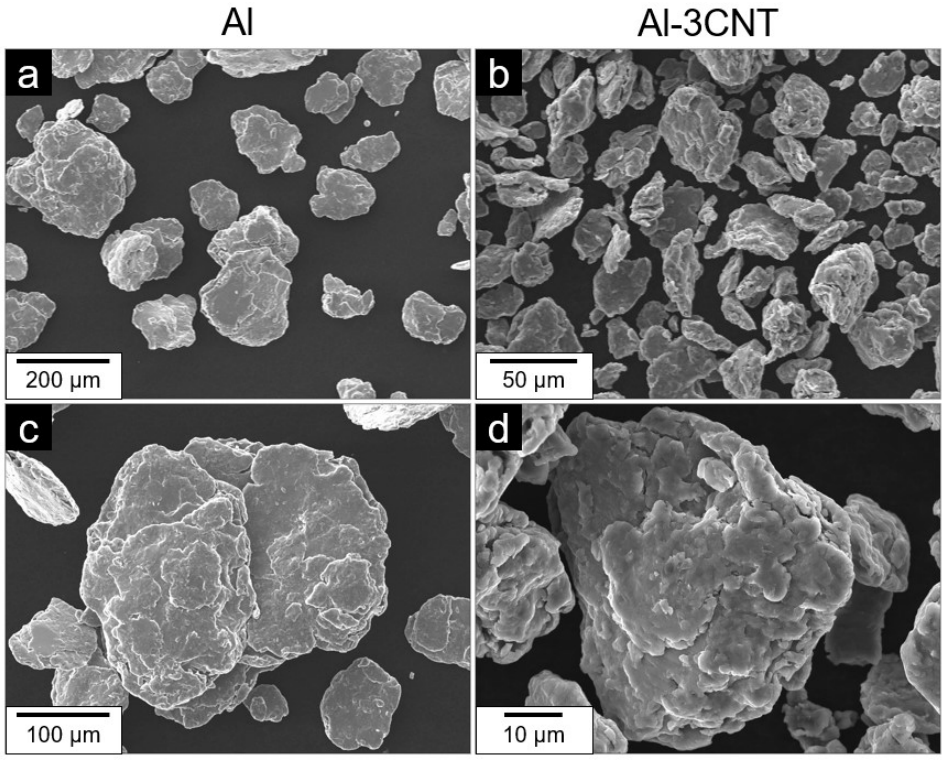

Fig. S1. Morphology of milled pure Al and Al-CNT composite powders. SEM images of (a,c) pure Al, (b,d) Al-3CNT powders at low (a,b) and high (c,d) magnification.

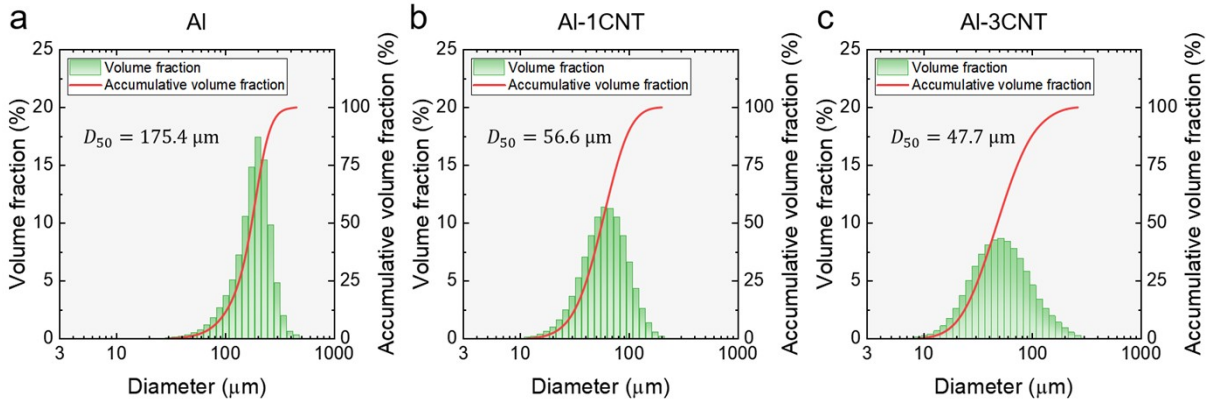

Fig. S2. Particle size distributions of pure Al and Al-CNT composite powders. Volume fraction and accumulative volume fraction as functions of particle diameter for (a) pure Al, (b) Al-1CNT and (c) Al-3CNT powders. D_{50} indicates the median particle diameter.

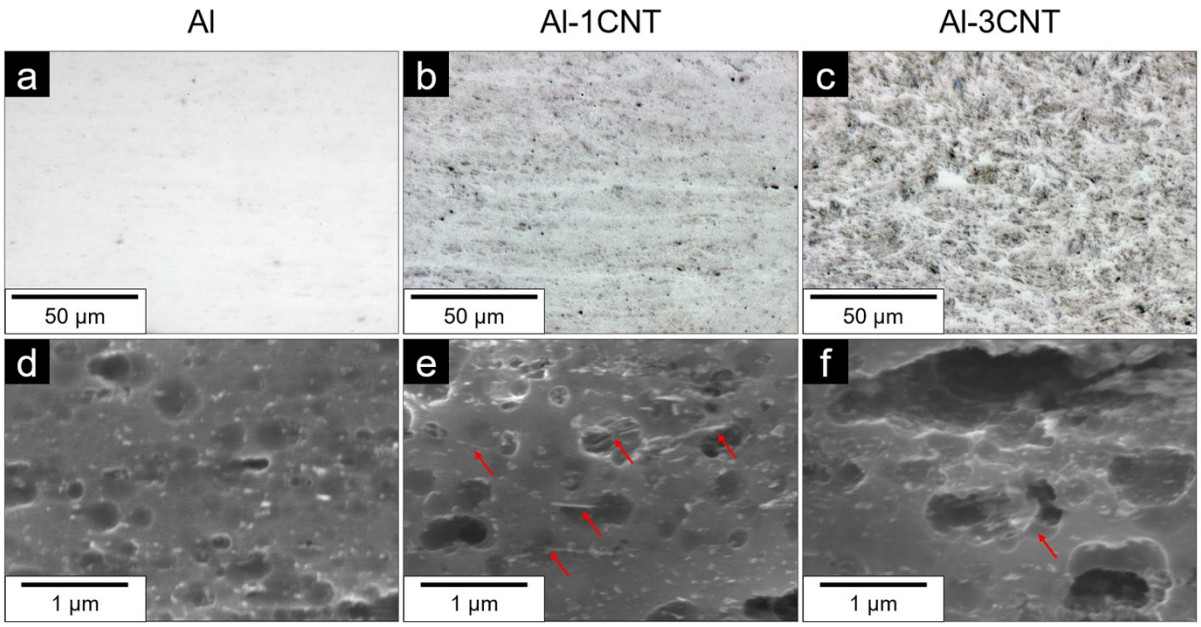

Fig. S3. Cross-sectional microstructure of rolled Al and Al-CNT composite. Optical micrographs of the as-polished specimens: (a) Al, (b) Al-1CNT, and (c) Al-3CNT. SEM images of the corresponding etched specimens: (d) Al, (e) Al-1CNT, and (f) Al-3CNT. Red arrows indicate CNTs. The etched condition after immersion in Keller's reagent (190 mL H_2O, 5 mL HNO_3, 3 mL HCl, and 2 mL HF) for 90 s.

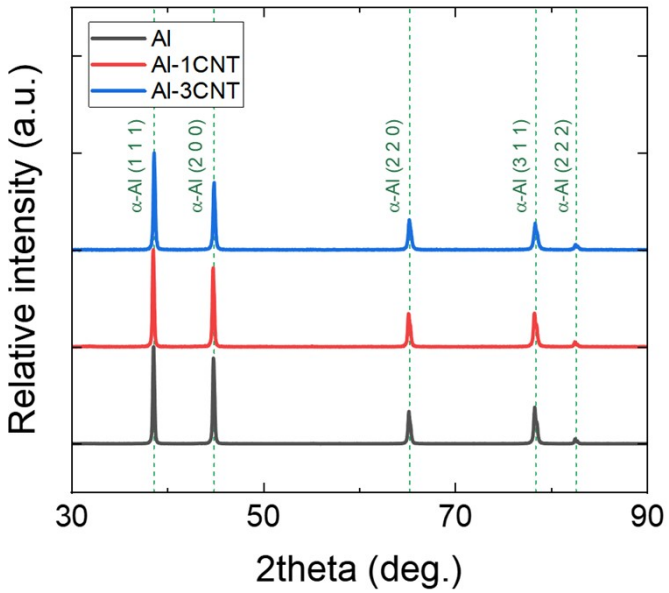

Fig. S4. X-ray diffraction patterns of as-rolled pure Al and Al-CNT composite foils.

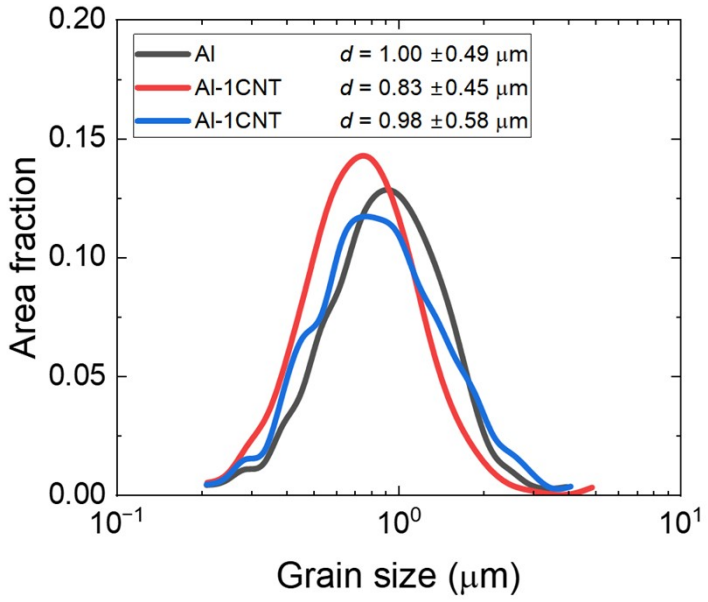

Fig. S5. Grain size distribution of as-rolled pure Al and Al-CNT composite foils.

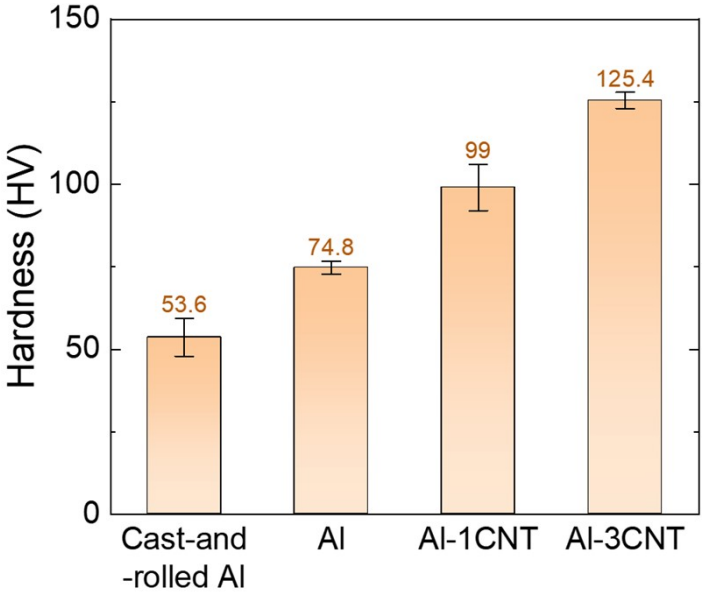

Fig. S6. Hardness of as-rolled pure Al and Al-CNT composite foils.

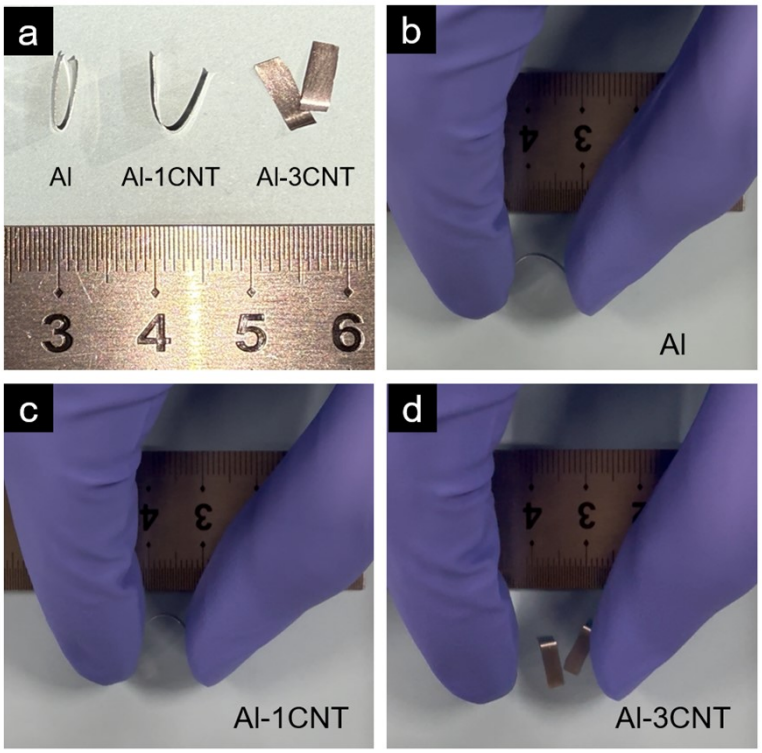

Fig. S7. Mechanical bend response of as-rolled pure Al and Al-CNT foils. (a) Photographs of Al foils after 180° bending. Configuration of (a) pure Al, (b) Al-1CNT, and (c) Al-3CNT foils during 180° bending.

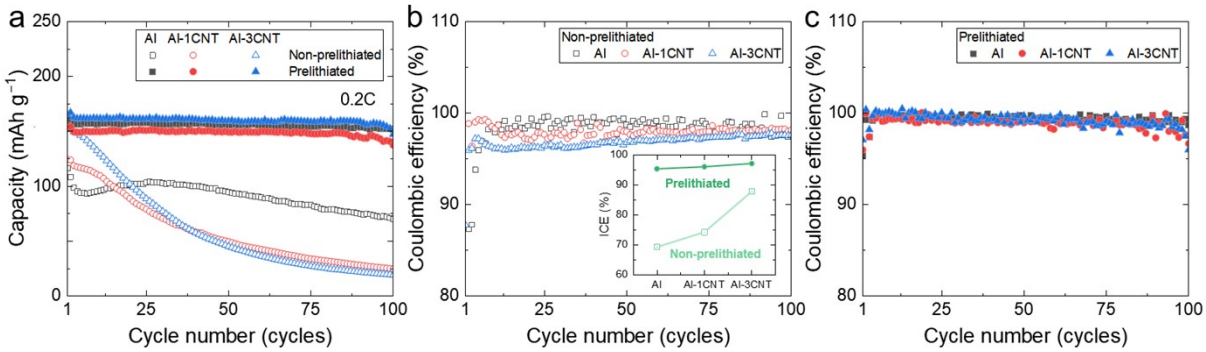

Fig. S8. Electrochemical performance of pure Al and Al–CNT anodes at high cathode loading. (a) Discharge capacity as a function of cycle number at a current density of 0.3 mA cm^{-2} with an LFP areal loading of 9.0 mg cm^{-2}. (b,c) Coulombic efficiency versus cycle number for non-prelithiated and prelithiated cells. The inset in (b) presents the initial coulombic efficiency (ICE) of the corresponding cells.

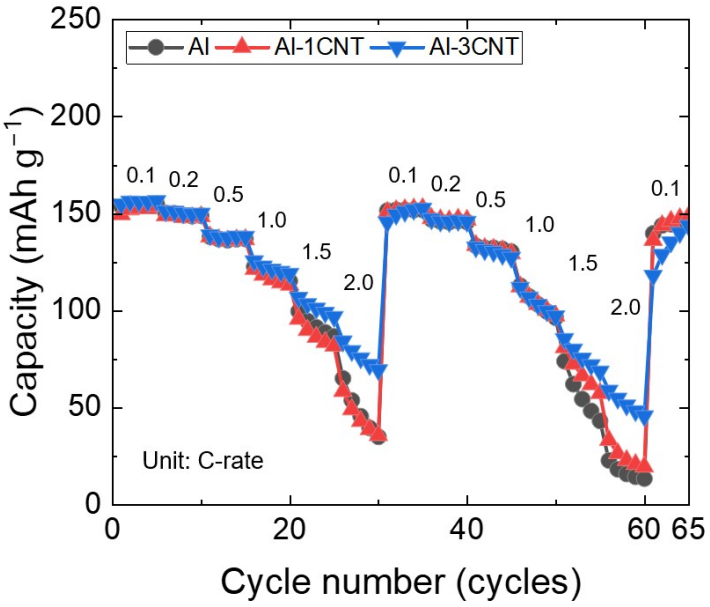

Fig. S9. Rate performance of LFP full cells with prelithiated pure Al and Al-CNT anodes. Discharge capacity versus cycle number at different C-rates, with the C-rate values indicated in the plot, for cells employing prelithiated pure Al, Al-1CNT and Al-3CNT anodes. LFP cathode areal loading 9.0 mg cm^{-2}.

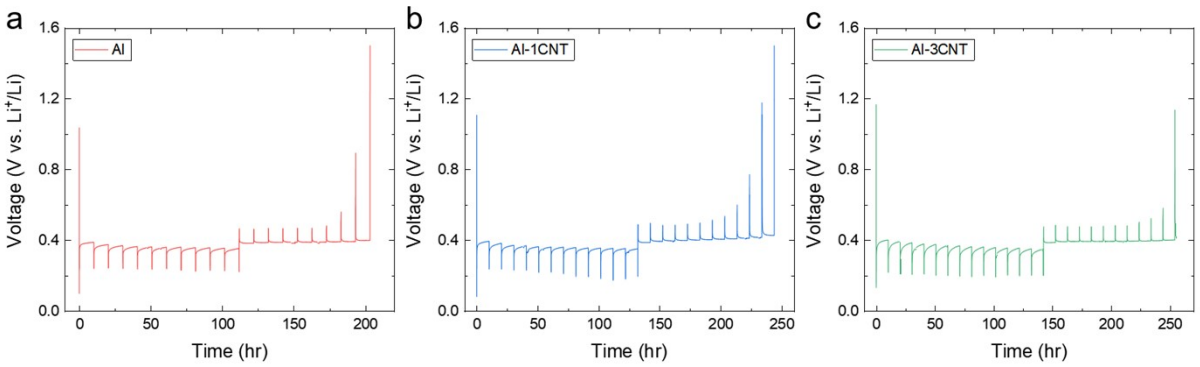

Fig. S10. Voltage profiles during GITT measurements. (a) Pure Al, (b) Al-1CNT, and (c) Al-3CNT during the first regular cycle under a limited lithium-inventory protocol at a current density of 0.3 mA cm^{-2}.

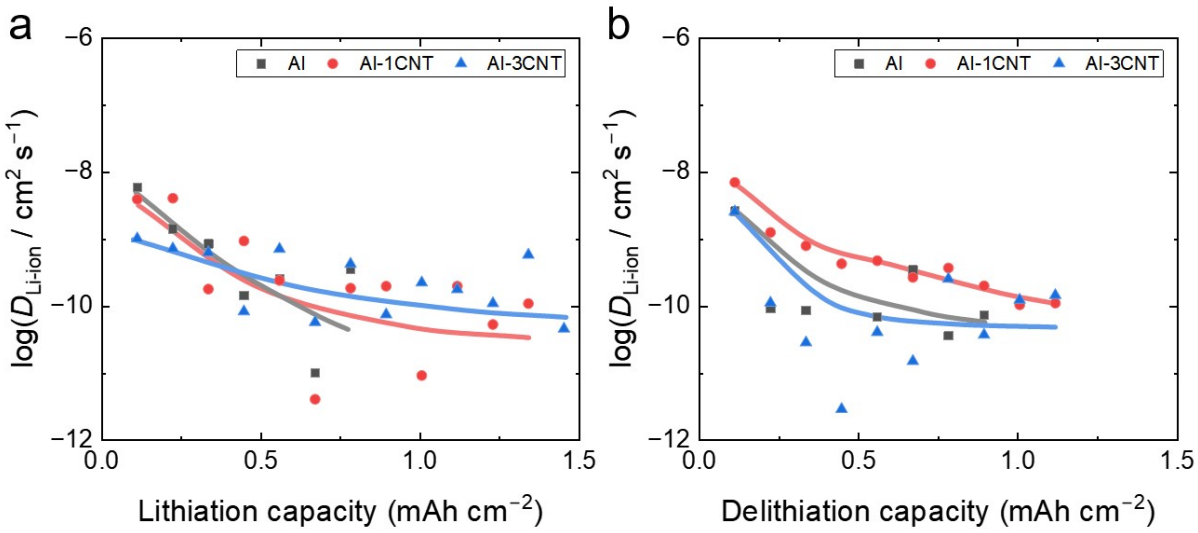

Fig. S11. Capacity-dependent Li-ion diffusivity from GITT during the first regular cycle. log($D_{Li\text{-}ion}$) is plotted as a function of (a) lithiation capacity and (b) delithiation capacity for pure Al, Al–1CNT, and Al–3CNT anodes. Apparent Li-ion diffusivity ($D_{Li\text{-}ion}$) extracted from GITT under the lithium-inventory protocol (initial lithiation capacity = 2 mAh cm^{-2}). Current densities were 0.2 mA cm^{-2} for the formation cycle and 0.67 mA cm^{-2} for the regular cycles. Symbols represent values calculated using Eq. (1).

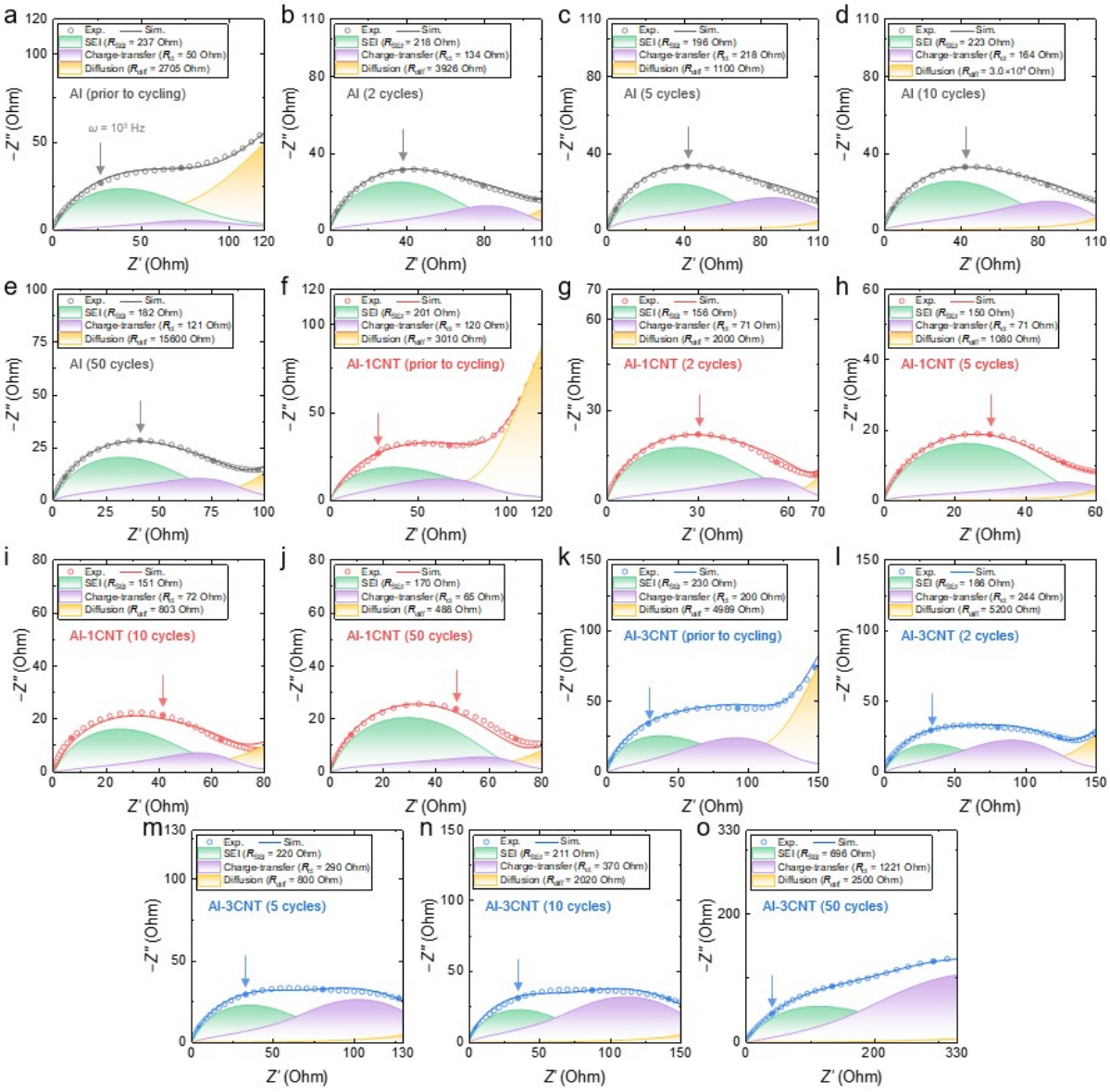

Fig. S12. Nyquist plots of electrochemical impedance spectra during cycling. Nyquist plots show experimental data and equivalent-circuit fits, with the fitted impedance contributions from the SEI, charge-transfer, and diffusion overlaid. Panels correspond to (a-e) Al, (f-j) Al–1CNT, and (k-o) Al–3CNT, measured in the (a,f,k) as-prelithiated state and after (b,h,l) 2, (c,I,m) 5, (d,i,n) 10, and (e,j,o) 50 galvanostatic cycles. Arrows indicate the high-frequency region, ~10^3 Hz.

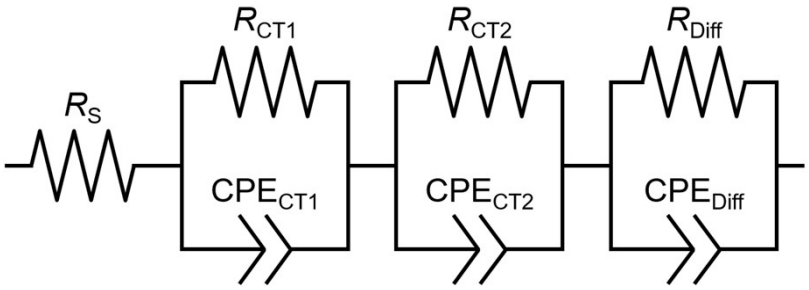

Fig. S13. Equivalent circuit used for fitting electrochemical impedance spectra.

Table S1. Chemical composition of the milled pure Al powder.

Element	Al	Si	Mn	Cu	Zn	Fe	Zr
Composition (wt%)	Balanced	0.004	0.001	0.044	0.001	0.089	0.002

Table S2. Binding energies used for XPS peak assignment. Al 2p, O 1s and F 1s core levels with the corresponding species, binding energies (B.E., eV) and references.

Al 2p			O 1s			F 1s		
Species	B.E. (eV)	Ref.	Species	B.E. (eV)	Ref.	Species	B.E. (eV)	Ref.
AlF_3	77.4	53	C–O	533.0	53	POF3	687-688.5	62
Al–O	74.6	54	O–C=O	532.7	58	LiPF6	687.0	63
Al–O–Li	73.9	55	O–O	531.5	59	AlF3	686.7	64
Al–C	72.4-73.2	56	Al–O	531.1	54	LiF	684-685.5	54
Al^0	72.6	54	Al–O–Li	530.0	60			
Al–Li	71.5	57	O^{2-}	528.5-529	61			

Table S3. XPS-derived surface atomic composition of Al and Al–CNT anodes. Atomic percentages (at.%).

Sample	Li	C	O	F	Al	Si	P
Non-prelithiated Al after formation cycle	23.62	21.61	23.89	19.70	8.56	0.62	2.00
Non-prelithiated Al-1CNT after formation cycle	24.44	25.71	18.47	22.88	5.19	0.47	2.84
As-prelithiated Al-1CNT	44.61	20.93	27.52	5.36	0.86	0.34	0.38
Prelithiated Al-1CNT after formation cycle	45.06	27.89	24.61	2.50	0.00	0.00	0.00